

High speed 2-dimensional temperature measurements of nanothermite composites: Probing thermal vs. Gas generation effects

Rohit J. Jacob, Dylan J. Kline, and Michael R. Zachariah

Citation: *Journal of Applied Physics* **123**, 115902 (2018); doi: 10.1063/1.5021890

View online: <https://doi.org/10.1063/1.5021890>

View Table of Contents: <http://aip.scitation.org/toc/jap/123/11>

Published by the *American Institute of Physics*

Articles you may be interested in

[Investigating the oxidation mechanism of tantalum nanoparticles at high heating rates](#)

Journal of Applied Physics **122**, 245901 (2017); 10.1063/1.4995574

[Integrating micro-ignitors with Al/Bi₂O₃/graphene oxide composite energetic films to realize tunable ignition performance](#)

Journal of Applied Physics **123**, 095305 (2018); 10.1063/1.5016576

[Incomplete reactions in nanothermite composites](#)

Journal of Applied Physics **121**, 054307 (2017); 10.1063/1.4974963

[First principles study of hydrogen bond symmetrization in \$\delta\$ -AlOOH](#)

Journal of Applied Physics **123**, 115901 (2018); 10.1063/1.5019586

[Bandgap profiling in CIGS solar cells via valence electron energy-loss spectroscopy](#)

Journal of Applied Physics **123**, 115703 (2018); 10.1063/1.5011658

[Shock interactions with heterogeneous energetic materials](#)

Journal of Applied Physics **123**, 105901 (2018); 10.1063/1.5022042

Quantum Design Brings You the Next Generation Magneto-Optic Cryostat

Only be limited by your imagination...

Room Temperature Window
Split-Coil Conical Magnet
Sample Pod
User Wiring Ports

Learn More

Quantum Design
qdusa.com/opticool5

8 Optical Access Ports: 7 Side; 1 Top
Temperature Range: 1.7 K to 350 K
7 T Split-Coil Conical Magnet
Low Vibration: <10 nm peak-to-peak
89 mm x 84 mm Sample Volume
Automated Temperature & Magnet Control
Cryogen Free

High speed 2-dimensional temperature measurements of nanothermite composites: Probing thermal vs. Gas generation effects

Rohit J. Jacob,^{1,2,a)} Dylan J. Kline,^{1,2,a)} and Michael R. Zachariah^{1,2,b)}

¹Department of Chemical and Biomolecular Engineering, University of Maryland, College Park, Maryland 20742, USA

²Department of Chemistry and Biochemistry, University of Maryland, College Park, Maryland 20742, USA

(Received 9 January 2018; accepted 20 February 2018; published online 16 March 2018)

This work investigates the reaction dynamics of metastable intermolecular composites through high speed spectrometry, pressure measurements, and high-speed color camera pyrometry. Eight mixtures including Al/CuO and Al/Fe₂O₃/xWO₃ (*x* being the oxidizer mol. %) were reacted in a constant volume pressure cell as a means of tuning gas release and adiabatic temperature. A direct correlation between gas release, peak pressure, and pressurization rate was observed, but it did not correlate with temperature. When WO₃ was varied as part of the stoichiometric oxidizer content, it was found that Al/Fe₂O₃/70% WO₃ achieved the highest pressures and shortest burn time despite a fairly constant temperature between mixtures, suggesting an interplay between the endothermic Fe₂O₃ decomposition and the higher adiabatic flame temperature sustained by the Al/WO₃ reaction in the composite. It is proposed that the lower ignition temperature of Al/WO₃ leads to the initiation of the composite and its higher flame temperature enhances the gasification of Fe₂O₃, thus improving advection and propagation as part of a feedback loop that drives the reaction. Direct evidence of such gas release promoting reactivity was obtained through high speed pyrometry videos of the reaction. These results set the stage for nanoenergetic materials that can be tuned for specific applications through carefully chosen oxidizer mixtures. *Published by AIP Publishing.*

<https://doi.org/10.1063/1.5021890>

I. INTRODUCTION

Research in nanoscience, as in many fields, has permeated the development of energetic materials where the demand for improved reactivity may be achieved with increased intimacy between reactants. Traditional monomolecular Carbon-Hydrogen-Nitrogen-Oxygen (CHNO) systems represent optimal reactant proximity, with mixing achieved at the molecular scale. However, the gaseous nature of their reaction products allow limited enhancements in their energy content.^{1,2} As a result, much recent research has been directed towards nano-scale composite energetic materials incorporating metal nanoparticles as fuel so as to enhance the energy content and release rate.³ One of the primary advantages of using metallic fuels is their high volumetric energy density leading to some metal based energetic materials having heats of reaction larger than the state of the art CHNO systems.¹ However, using non-molecular, fuel-oxidizer systems implies a diffusion-limited process. It has been demonstrated repeatedly that the use of nanoparticles, with decreased length scale, leads to a metastable system with orders of magnitude improvement in reactivity compared to their counterparts mixed at coarser scales.⁴ A large body of recent research has been directed at exploring the underlying mechanism responsible for the fast reaction rates observed in such Metastable Intermolecular Composites (MIC)/nanothermite combustion, with the general consensus being that the dominant energy transfer mechanism in MIC powder is convection and molten particle advection⁵ and the

primary mode of ignition/reaction is via the condensed phase diffusion of reactant moieties.^{6,7}

A significant benefit of MIC systems is their tunability, which stems from the extensive permutations in the selections of fuels, oxidizers,^{8,9} gas generators,¹⁰ and architecture,^{11,12} with the state of the art systems showing flame speeds as high as 4000 m/s.¹³ Several methods have been developed to quantify their reaction dynamics with, ignition temperature and speciation measurements,^{8,14} thermo-analytical methods,¹⁵ flame speeds,¹⁶ thermo-equilibrium software (CEA, Cheetah),¹⁷ and constant volume combustion¹⁸ being the most common. Although these methods do help in quantifying the combustion characteristics of MIC's, the flame speed and pressure measurements are significantly affected by variations in their experimental design. Temperature, on the other hand, is a fundamental thermodynamic property and is directly related to energy release, although its measurement in energetic materials research is not as prevalent as one might suppose. Primarily, the wide range of reaction times (10 μs–100 ms), temperature range (800 K–over 4000 K), and spatial inhomogeneity make robust temperature measurements a challenge. Moreover, MIC's have significant emission interference from atomic and molecular species that participate in the high temperature reaction, thereby reducing the applicability of broadband measurement techniques.

Despite these limitations and challenges, the non-invasiveness and relative simplicity of emission measurements as compared to other optical methods and the artifacts introduced by traditional invasive methods mean that optical emission is preferred for MIC characterization. Weismiller *et al.*¹⁹

^{a)}R. J. Jacob and D. J. Kline contributed equally to this work.

^{b)}Author to whom correspondence should be addressed: mrz@umd.edu

studied three different nanothermite compositions in an unconfined pile, and confined burn tube using multi-wavelength pyrometry. Kappagantula *et al.*²⁰ also examined several Al/CuO and Al/PTFE based composites with metal additives using an IR camera as a means to optically measure performance. Despite the assortment of temperature measurement methods used to observe these energetic compounds, a common theme in each experiment was the inability for the compound to achieve its adiabatic flame temperature. The similarity across different composite mixtures has supported the conclusion that the systems under study were limited by the melting and decomposition of the oxide. Through such insights into the reaction dynamics, it might be possible to tune the reactivity of composite materials by altering the participation of competing reactions through mixture content variation. Prior work by Sullivan and Zachariah²¹ first explored this possibility by incrementally adding nanoscale WO_3 to an Al/ Fe_2O_3 nanothermite to demonstrate an increase in the pressurization rate under a constant volume combustion environment. The result was counterintuitive as gas generation was observed to increase with the reduction of gas generating species (Fe_2O_3) in the composite. The Al/ Fe_2O_3 nanothermite was postulated to be rate limited by oxidizer decomposition, and the performance improvement was attributed to efficient decomposition of Fe_2O_3 induced by the heightened flame temperature at higher WO_3 concentrations. While the results were corroborated with equilibrium calculations, no direct temperature measurement was made to support the claims regarding the interplay of reaction mechanisms. The purpose of this work is to extend the results of Sullivan and Zachariah²¹ through high-speed, multi-wavelength pyrometry to probe the tunable reactivity of a nanothermite composite in a closed pressure vessel. Moreover, the effects of enhanced gas production on reactivity are visualized under unconfined conditions with high spatial and temporal resolution using high speed color camera pyrometry.

II. EXPERIMENTAL

A. Materials and sample preparation

Commercially available aluminum nanoparticles (ALEX, Argonide Corp.) with an active content of 68.7 wt. % (from

thermogravimetric analysis) and an average particle size of 50 nm were used in this study. The oxide nanopowders (CuO , WO_3 , and Fe_2O_3) were procured from Sigma Aldrich and all had average diameters <100 nm. The samples were prepared by dispersing a known amount of oxide in 10 ml of hexane and sonicating in an ultrasonic bath for an hour. This was done in order to break down the soft aggregates, ensuring better mixing with the fuel. A stoichiometric amount of aluminum was then added to this slurry and further sonicated for an hour. The slurry was left overnight to dry. The dry sample was gently scraped off the vial and broken up using a grounded spatula until powder consistency was achieved. Samples prepared included stoichiometric blends of Al/CuO, Al/ Fe_2O_3 , and Al/ WO_3 . Additionally, a set of 5 samples were made where we systematically adjusted the oxidizer composition by adding 20%, 60%, 70%, 80%, and 90% by mole of WO_3 to the Fe_2O_3 system, while maintaining the overall stoichiometry of the blend as outlined in the prior work by Sullivan and Zachariah.²¹ For experiments involving high-speed videography, the slurry was kept as it is for drop casting on a fine platinum wire for rapid heating, as discussed in Sec. II D.

B. Constant volume combustion cell

The constant volume pressure cell used is described in detail elsewhere.^{21,22} Briefly, the cell is a closed reaction vessel with a free volume of ~ 20 cm³, equipped with 3 ports (as shown in Fig. 1). One port houses a high frequency pressure transducer (PCB Piezoelectronics) for measuring the pressure signal generated during sample ignition and combustion. The second port is connected to an optical assembly used for collecting broadband emission from the inner edge of the vessel. The optical assembly consists of a plano convex lens (Thorlabs) which collects and focuses the light from the vessel into a 2 m long fiber optic cable (Dia. 1 mm, Thorlabs Inc.) coupled to a photomultiplier tube (PMT) (Hamamatsu). An optional neutral density filter (Thorlabs Inc.) is placed between the lens and the fiber for significantly brighter samples so as to prevent saturation of the detector. Both the PMT and the pressure transducer outputs are connected to a digital oscilloscope (Teledyne LeCroy Wavesurfer 3000) sampled at

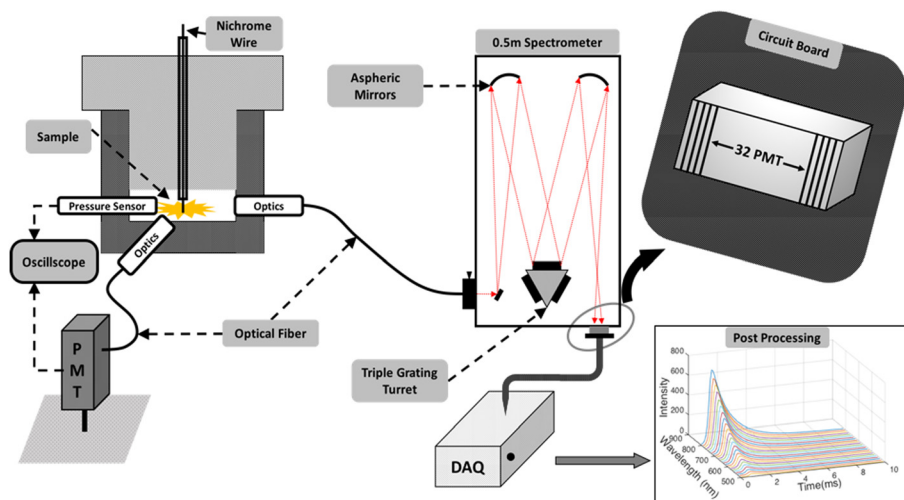


FIG. 1. Schematic of the experiment consisting of the pressure cell and attached diagnostics. The pressure cell is shown on the left. The spectrometer is coupled to the pressure cell via an optical fiber. The light from the fiber is spectrally dispersed by the selected grating on the turret which is subsequently imaged on the 32 channel PMT and digitized using the Data Acquisition system (DAQ). The digitized data is processed to produce time resolved spectra.

5 MHz. The PMT's cathode voltage is selected empirically by monitoring the output current during trial tests. The third port houses another optical assembly which collects and relays the emission to a spectrometer, which is detailed in Sec. II C. The cell was placed inside an artificial environment bag which was purged with argon to mitigate the influence of atmospheric oxygen on the reaction.

Each sample (25 mg) was tested in triplicate by ignition with a resistively heated nichrome wire connected to a DC power supply. A custom square wave generator was built in-house to simultaneously trigger the spectrometer, oscilloscope, and the power supply for the nichrome wire. Owing to the high temperatures and significant production of gas and condensed species, a sapphire window was used to protect the optical assembly and was cleaned periodically so as to ensure accurate measurement of the emission.

C. High speed 32-channel spectrometer

The optical assembly interfacing the spectrometer with the pressure cell consists of a Sapphire window, a Plano Convex lens $1f$ from the inner edge of the vessel, a neutral density filter (ND2), and a 455 nm color glass filter for order sorting. The optical components are assembled inside a 0.5 in. lens tube and the end of the tube is closed with a Sub-Miniature Assembly (SMA) fiber optic adapter. The plano-convex lens collimates the light from the inner edge of the vessel which is subsequently attenuated by either an ND1 or ND2 filter depending on the brightness of the reaction. A 1 mm diameter optical fiber (Princeton Instruments) transmits the emission into a 500 mm, triple grating, Czerny-Turner Imaging spectrometer (Acton SP 500i), as shown in Fig. 1. A 150 groove/mm grating and a slit width of 100 μm were chosen for this work, which gave a dispersion of 13 nm/mm at the focal plane and a spectral range of 464–867 nm. The primary objective of this work was to detect temperature; hence, a low-resolution grating was chosen so as to obtain the widest spectrum.

The spectrometer outlet was coupled with a 32 channel PMT module (Hamamatsu, H7260) with each channel having a dimension of 0.8 mm \times 7 mm (W \times H), implying a spectral resolution of ~ 10 nm/channel. A PMT-based detector was preferred in this work for its fast rise time (0.6 ns), tunable supply voltage (400–900 V), and single photon efficiency. The multichannel PMT (MC-PMT) is interfaced with a high-speed data acquisition (DAQ) system (Vertilon IQSP580) which terminates the MC-PMT to 50 Ω and measures the current output at the anode with 14-bit resolution. The system is capable of sampling at a maximum rate of ~ 390 kHz with an onboard storage for 5×10^5 32 channel events. With a temporal interval of ~ 2.5 μs , the current setup offers a good compromise between time resolution and total recording time, particularly for the combustion of nanothermites which are not only much slower than explosives, but also have a wide range of combustion time scales. One of the significant limitations of the setup is the 20 μA linearity limit of the MC-PMT, which limits the dynamic range of detection. This is offset by running multiple experiments where the ND2 filter, used for characterizing the emission at peak

irradiances, was replaced with a ND1 for characterizing the cooler phases of the reaction.

Wavelength calibration for the 32-channel spectrometer was performed using an HgNe pencil lamp (Newport) and spectral response calibration was performed with a calibrated tungsten halogen lamp (Avantes HAL CAL) operating at 2440 K. To test the linearity of the MC-PMT, a high temperature blackbody source operated at 1273 K was used and the signal was attenuated with neutral density filters (ND 0.4, ND 1). A detailed description of the calibration process and its results are provided in the [supplementary material](#) of this report. In order to make quantitative temperature measurements, the corrected data from the MC-PMT was linearized^{23–25} according to Wein's law as shown in Eq. (2), where ϵ : emissivity, h : Planck's constant, c : speed of light, K : Boltzmann constant, T : temperature, L : radiance, $C_{1,2}$: first and second radiation constant, and λ : wavelength. Wein's Law is a derivative of Planck's Law [Eq. (1)] and is applicable when the product $\lambda T < 3000$ $\mu\text{m K}$,²⁴ satisfied by visible emission true for most energetic material combustion. Once the parameter Z is calculated, it is plotted against the wavelength and a straight-line fit is employed to calculate the temperature

$$L(\lambda, T) = \frac{\epsilon * 2\pi hc^2}{\lambda^5 \left\{ \exp\left(\frac{hc}{\lambda KT}\right) - 1 \right\}}, \quad (1)$$

$$Z = \frac{\lambda}{C_2} \log\left(\frac{C_1}{\lambda^5 I}\right) = -\frac{\lambda}{C_2} \log \epsilon + \frac{1}{T}. \quad (2)$$

Implicit in the above linearization is the grey body assumption for the flame cloud generated by the reaction, of which there has been considerable debate in the community. Some authors have employed the $\epsilon \sim \lambda^{-1}$ dependence^{19,26} which is derived from the spectral dependence of the absorption efficiency in the Rayleigh limit, while neglecting the spectral dependence of the absorption index. Others have corrected this correlation by incorporating the inverse wavelength dependence of the absorptive index, thereby resulting in a $\epsilon \sim \lambda^{-2}$ correlation.²⁷ Recent efforts by Lynch *et al.* have suggested that under conditions where the high temperature flame front is optically thick, which presumably would be the case in a confined reaction, the gray body assumption could be valid, and hence is used in this study.²⁸ During the temperature fitting procedure, channels with spectral band-pass that overlapped prominent molecular emission, such as Na doublet (588.95 nm and 589.59 nm) and AIO band ($\Delta v = -1, 0, +1, 464$ nm–530 nm), were removed so as to improve the fit fidelity. Built-in MATLAB fitting routines were employed to estimate the final temperature along with error bounds thresholded at ± 400 K.

D. Hot-wire ignition tests for spatiotemporal temperature maps

While the experimental setup including the spectrometer described above can measure the temperature of radiating particles using multi-wavelength techniques, its ability to measure the spatial dynamics of the combustion process is

limited by means of its data acquisition. Owing to the nature of light collection through an optical fiber, the spectrometer would be biased to the brightest/hottest spots within the flame due to the exponential scaling of light intensity with temperature as per the Stefan-Boltzmann Law. Furthermore, due to the spatially dynamic nature of the flame front, point light sources could constantly move in and out of the field of view, affecting the temperature measurement. As a complementary diagnostic to the spectrometer, a high-speed color camera is used to record videos of the combustion event so as to probe the highly dynamic flame front. A color camera operates by generating a mosaic of the scene under observation through selective bandpass transmission of light by the Bayer filter mask overlaid on the camera's CMOS sensor. This results in each pixel recording one color among red, green, and blue. Further processing by the camera software "demosaics" the data, generating RGB values at each pixel, to produce the image. Densmore *et al.* detailed how to employ a high speed color camera as a ratio pyrometer, which served as the basis for these experiments.²⁹

To calibrate the Vision Research Phantom Miro M110, videos of both a blackbody source (Newport Oriel 6700 Series) and a calibrated lamp (Avantes) were recorded while varying temperature. MATLAB was used for pixel extraction and then demosaiced using the built-in functions. Ratios for theoretical pixel intensity were then calculated for the calibration temperature with Eq. (3) [where I_i is the intensity of a channel, χ_i is the spectral response of the channel as a function of wavelength, ψ_i is channel gain, and the radiance L is given by Eq. (1)]. Calibration factors (C_{ij}) were then calculated by comparing the measured values to the theoretical ones as shown by Eq. (4) (where $C_{ij} = \psi_i/\psi_j$). A detailed description of the calibration process can be seen in the [supplementary material](#) section

$$\frac{I_i}{I_j} = \frac{\psi_i \int L(\lambda, T) \chi_i(\lambda) d\lambda}{\psi_j \int L(\lambda, T) \chi_j(\lambda) d\lambda}, \quad (3)$$

$$\left(\frac{I_i}{I_j}\right)_{exp} = C_{ij} \left(\frac{I_i}{I_j}\right)_{theor}. \quad (4)$$

Raw pixel values were extracted from the video files using a custom MATLAB script and were demosaiced to recover values for the red, green, and blue channels at each pixel, from which three ratios (green/red, blue/green, and blue/red), incorporating an inverse wavelength dependence of emissivity, were derived. To determine temperature, the calibration factors [from Eq. (4)] that account for the spectral response of the sensor were applied to three ratios and matched to the theoretical curves with a minimization algorithm. Although color camera pyrometry does allow for spatiotemporal measurements of temperature, limitations in the method by which raw data is collected are a strong source of error ultimately leading to deviations in temperature measurement from those reported by the spectrometer. Of the many elements that emit in the visible region during thermal relaxation, sodium is often the most noticeable with strong,

persistent lines seen as a doublet at 588.95 nm and 589.59 nm.³⁰ Such emission contributes to the red and green channel intensities, due to their high spectral response at these wavelengths ([supplementary material](#) Fig. S2), leading to error in temperature calculations. Other elements that have strong emission and are possible sources of contaminants in the experiments performed include potassium and copper. Furthermore, the calculations detailed above fails to account for light scattering from small particulates that may be generated throughout the course of the reaction. Hence, in order to maintain fidelity, the error minimization algorithm used to calculate temperature is error thresholded to ~ 100 K and the pixels that report higher errors are excluded from the final false-color images.

Wire ignition experiments were conducted in a stainless steel 6-way cross, with windows to visualize the combustion with the high-speed camera ([supplementary material](#) Fig. S4). The interior of the chamber was painted black in order to minimize light reflections. A premixed slurry of thermite samples were coated onto a 76 μm -diameter platinum wire and resistively heated in a 1 atm argon environment for 4 ms at a rate of $\approx 10^5$ K/s using the T-Jump apparatus detailed by Zhou *et al.*¹⁴ Two videos were recorded per sample at a framerate of 20,000 fps with the $f/\#$ and exposure times empirically chosen to provide the best signal to noise ratio.

III. RESULTS

A. Al/CuO nanothermite tests in the pressure cell

As a control system, we begin with the most studied thermite system Al/CuO. Figure 2 shows the temporal pressure response, normalized-integrated radiance across all PMT channels [Fig. 2(a)], and the temperature fit [Fig. 2(b)] for the Al/CuO reaction in the pressure cell. The peak pressure of the system is ~ 741 kPa and the pressurization rate is ~ 118 kPa/ μs , calculated based on the rise time of the first pressure peak. The temporal temperature profile shown in Fig. 2(b) is recorded using the ND2 Neutral density filter in order to quantify the emission at peak light intensity. The custom fitting algorithm enabled the simultaneous calculation of temperature, and the error associated with the fit which was thresholded to ± 400 K before plotting the profile shown in Fig. 2(b). The missing data points at longer durations correspond to such cases where the calculated error was higher than the threshold value. The figure is horizontally sectioned by gridlines so as to qualitatively analyze the different regimes.

Owing to the error thresholding, the first temperature data point was obtained at ~ 0.005 ms from ignition, where the integrated emission is approx. 15% of the peak integrated intensity. The pressure trace at this point corresponds to the first local maxima, as highlighted by the vertical line 1. Region 1–2 corresponds to a reduction in pressure accompanied by a temperature rise to ~ 3600 K which is followed by a sharp drop to ~ 2800 K in region 2–3. This coincides with an increase in pressure to its maximum value at ~ 0.017 ms (location 3) and the emission intensity is observed to have a sharp positive slope from point 2 onwards. At the instance of peak pressure, the normalized emission is $\sim 30\%$ and the

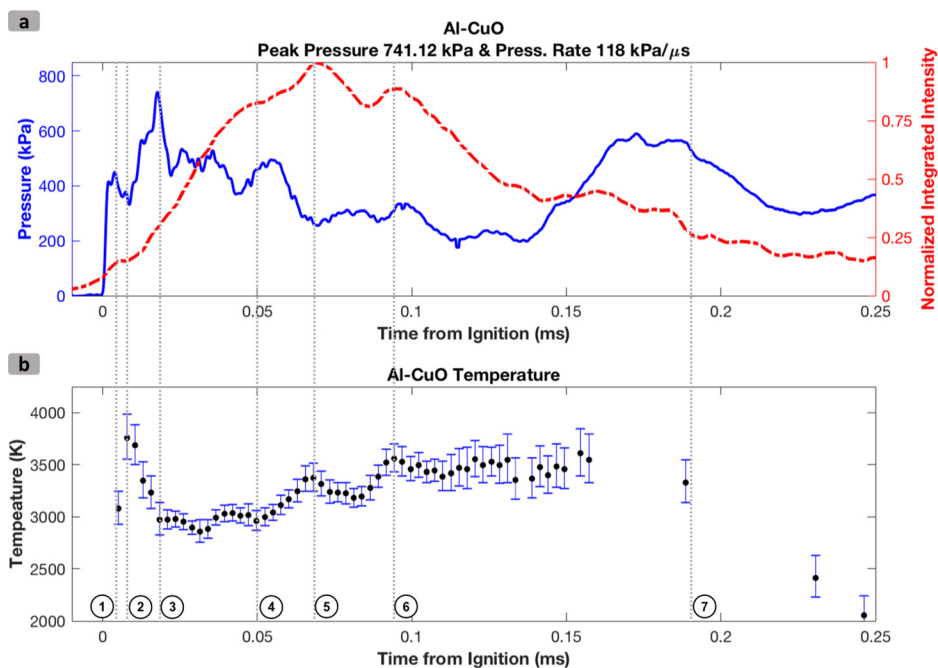


FIG. 2. Al/CuO nanothermite in the pressure cell. (a) Pressure-normalized-integrated intensity profile and (b) temporal reaction temperature profile. Region 1–2: temperature rise and pressure drop; 2–3: temperature drop and peak pressure; 3–4: rapid rise in integrated intensity at a constant temperature with decreasing pressure; 4–6: broadly represents increase temperature; 6–7: region with temperature plateau, decreasing integrated intensity, and pressure.

temperature is near the adiabatic flame temperature for Al + CuO (2837 K).²¹ Region 3–4 corresponds to the most substantial increase in integrated intensity as it rises from 30% to 80% at 0.05 ms (location 4), although the temperature in this region is observed to plateau at \sim 3000 K. The pressure profile, on the other hand, shows a steady decline in this region. Region 4–6 broadly corresponds to an increase in temperature to \sim 3500 K (location 6) and the emission intensity is observed to first increase in the region 4–5 by \sim 20%, attaining its peak at location 5. Region 5–6 continues the increasing trend of temperature although the integrated intensity is observed to drop by \sim 25%, achieving a local maximum at location 6, corroborated with an increase in temperature. In region 6–7, the emission intensity is observed to decline although the temperature profile is essentially plateaued at \sim 3500 K. Measurements beyond this point resulted in high errors due to low signal and were thresholded at \pm 400 K. The pressure signal is observed to continue its decline, although at 0.17 ms, a spike is observed which is the reflected pressure wave from the initial pressure spike. Such damped reflections were observed over a period of \sim 150 μ s, approximately the time it takes a sound wave to traverse twice the diameter of the cell. A lack of deviation in the measured temperature suggests the same, as a change in the combustion mechanism would have manifested in the measured temperatures. Qualitatively similar profiles were observed for repeat runs as well and the significance of each regime is discussed in more detail in the mechanism section. For measuring temperatures at longer durations, where the emission intensity is lower, a complementary test without employing the ND2 filter was done and the result is presented in the [supplementary material](#) Fig. S5.

Curiously, the integrated intensity [as shown in regions 5–7 of Fig. 2(a)] is observed to decline gradually after reaching the maximum, although the recorded temperature is still observed to increase/plateau. A possible explanation for this

observation could be that the flame cloud could have disintegrated into individual emitters which subsequently attenuate the net emission from the reaction due to the reduction in the emission area. Since the lens assembly is focused at the inner edge of the cell, and given that the temperature is seen to rise, we believe the spectrometer observes the combustion of such individual emitters which could be sintered reactants scattered by the initial pressure pulse.

B. Al/Fe₂O₃ and Al/WO₃ nanothermite tests in the pressure cell

The principal focus of this work is to infer the role of temperature in the tunable reactivity of nanothermites, specifically for the Al/Fe₂O₃ nanocomposite doped systematically with WO₃ nanoparticles. The pressure-temperature profiles for select samples are shown in Fig. 3, and quantitative comparison for the full suite of samples are shown in Fig. 4. As can be seen in Fig. 3(a) for the Al/Fe₂O₃ sample, the pressure profile is characterized by slow buildup which achieves the peak pressure \sim 10 ms after ignition. Such poor performance is again highlighted in Fig. 4(c), where the average Full Width Half-Max (FWHM) burn time is plotted against the composition, with Al/Fe₂O₃ being the slowest burning composite at 5.5 ms. With incremental addition of WO₃, the performance of the composite improves significantly, exemplified by the faster pressure buildup (Fig. 3), higher pressurization rate [Fig. 4(b)], and much shorter burn time, as shown in Fig. 4(c). With the increase of WO₃ concentration in the composite, the pressure and pressurization rates are observed to increase till it reaches an optimum value at \sim 70% WO₃ [Fig. 4(b)] beyond which any addition of WO₃ resulted in the detriment of the reactivity. For Al/WO₃, the observed pressure buildup was slower than that of the composites with mixed oxides although it is still faster

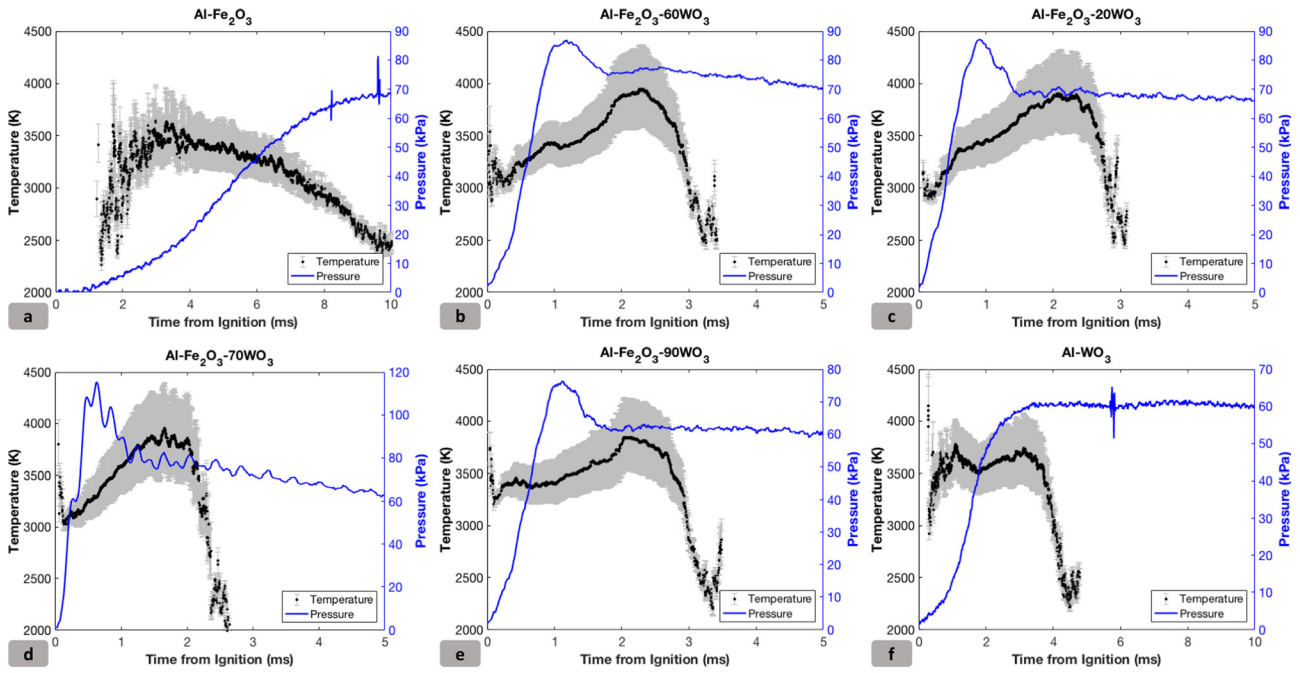


FIG. 3. Temporal pressure-temperature profiles for (a) Al-Fe₂O₃, (b) Al-Fe₂O₃-20WO₃, (c) Al-Fe₂O₃-60WO₃, (d) Al-Fe₂O₃-70WO₃, (e) Al-Fe₂O₃-90WO₃, and (f) Al-WO₃ in the pressure cell. The grey region is the error bound of the measurement.

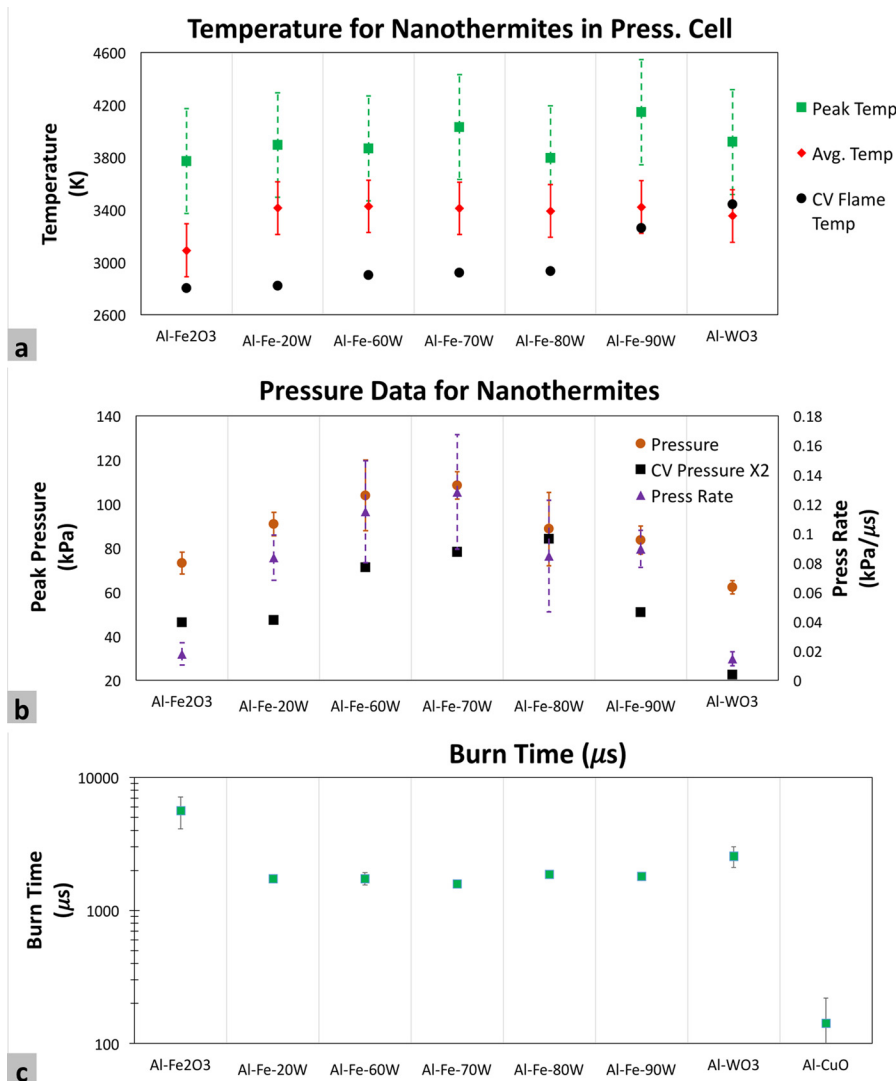


FIG. 4. Pressure-temperature profiles for (a) effect of composition on temperature, (b) effect of composition on pressure and pressurization rate (Al/CuO: $P_{max} = 572$ kPa and Press. Rate = 41 kPa/ μ s), and (c) effect of composition on burn time.

than Al/Fe₂O₃, suggestive of higher reactivity as demonstrated by its shorter burn time compared to Al/Fe₂O₃ (2.5 ms vs 5.5 ms). The lack of any gas phase products for the Al/WO₃ reaction⁸ explains its poor pressure metrics among all the composites. The qualitative difference between the respective plots would be analyzed in more detail from a mechanistic standpoint in Sec. IV.

The quantitative metrics for the full suite of samples tested in this study, averaged over 3 runs, is presented in Fig. 4. Theoretical estimates of the temperature and pressure under constant volume conditions, calculated using NASA CEA, are also presented for comparison. Figure 4(a) highlights the effect of composition on temperature thresholded to a standard error of ± 400 K, as it was the maximum error allowed in these measurements. With the addition of minimal amounts of WO₃, the average temperatures are seen to rise and plateau at around 3400 K which corresponds to the adiabatic flame temperature of Al/WO₃ (3447 K),²¹ and is slightly higher than the temperature for full Fe₂O₃ decomposition. The peak temperatures, on the other hand, are seen to rise gradually with added WO₃ until they reach a local maximum at 70%WO₃, although the high errors associated with peak temperatures preclude further discussion. Figure 4(c) compares the average FWHM burn times for all composites, with Al/Fe₂O₃ not surprisingly being the slowest (~ 5.5 ms) and Al/CuO the fastest (~ 150 μ s). The other composites show a steady burn time of ~ 2 ms. Al/Fe₂O₃/70WO₃ had the shortest burn time in the pressure cell tests, although it is difficult to distinguish on the logarithmic scale. The error bars associated with the burn time measurements were, in some cases, smaller than the marker themselves. Al/CuO pressure data is not shown in Fig. 4(b) owing to its large magnitude ($P_{max} = 572$ kPa and Press. Rate = 41 kPa/ μ s) which skews the pressure profile, inhibiting visual comparison.

C. Qualitative observation of reaction dynamics with camera

High speed color camera pyrometry videos enabled the identification of the different mechanisms of Al/Fe₂O₃, Al/Fe₂O₃/*x*WO₃, and Al/WO₃ reactions due to distinct features that appeared throughout the reaction. For the Al/Fe₂O₃ mixture, the gas release from the thermite mixture produced a cloud of reacted material and little unreacted material was left as it propagated down the wire [Fig. 5(a)]. The Al/Fe₂O₃ reaction is believed to be limited by the oxidizer decomposition, and is characterized by the slow reaction of the aluminum with gas phase oxygen released from the oxidizer, as exemplified by its longer burn durations and slow rising pressure profile.^{8,21} In comparison, the Al/WO₃ reaction is expected to occur in the condensed phase due to the lack of oxygen release from WO₃.⁸ Upon observing the videos of the Al/WO₃ reaction, the condensed phase nature of this reaction was evident by the absence of a reactive cloud, as the reaction seemingly occurred on the wire and continued on to the ends after melting the wire [Fig. 5(c)]. In line with the observations from the pressure cell, the Al/Fe₂O₃/70%WO₃ sample [Fig. 5(b)] shows both higher peak temperature, and a larger combustion zone which we attribute to

higher gas release. The use of a color camera to measure temperature allows for the direct observation of the disaggregating role that the oxidizer gas release plays during the reaction since the reaction cloud exhibits higher temperatures than the material remaining on the wire.

IV. MECHANISM

A large body of previous work has been devoted to the mechanistic examination of the Al/CuO system and is only briefly described here. It has been shown through high resolution microscopy that the Al/CuO system initiates in the condensed phase³¹ where the reactants are postulated to undergo reactive sintering. Based on the observed pressure, emission, and temperature profile, we propose the following mechanism for the Al/CuO system. Upon ignition, the temperature observed in Fig. 2(b) is close to the adiabatic flame temperature (T_{ad}) of Al/CuO (2837 K)²¹ and rises as the pressure wave unloads (region 1–2), with gas phase reactions between aluminum and oxygen, from the decomposition of CuO, dominating the combustion (region 1–2). Due to this spike in temperature, the unreacted copper oxide would undergo endothermic decomposition (as highlighted by the reduction in temperature in region 2–3), producing gaseous oxygen and a rise in pressure. This promotes advection which ignites the bulk sample and continues to burn in the region 3–4, where temperatures measured are close to the T_{ad} . The gas generation and unreacted material ignition is a symbiotic process and leads to bulk overall combustion as exemplified by the sharp increase in the emission intensity in the region 3–4.

We believe that the dominant reaction pathway in this region is in the condensed phase through reactive sintering^{6,7} as evidenced by large reaction products that are known to form.⁷ The rising temperature in region 4–6 results from oxygen released from the decomposition of CuO reacting with Al. The most clear evidence for this is that the observed temperatures at ~ 3500 K exceed the adiabatic flame temperature of Al/CuO and thus implies that aluminum, which sinters into super-micron particles, behaves like micron aluminum burning in oxygen.³² Region 6–7 is characterized by a temperature plateau at ~ 3500 K which could be attributed to the combustion of such aggregates, similar to those observed in extended length burn tube tests.³³ The maximum achievable spectral resolution of this instrument is 1 nm/channel (using a 1800 l/mm grating) which is low for resolving the AlO emission band, a common signature of gas phase combustion of aluminum particles, and hence was not adopted in this study.²⁸

In comparison to Al/CuO, the Al/Fe₂O₃ reaction is limited by the slow decomposition of the iron oxide into gas phase oxygen, which leads to prolonged emission traces and slow pressurization rates. The Al/WO₃ reaction is expected to occur entirely in the condensed phase as the WO₃ produces no gas phase decomposition products. Such qualitative differences can be readily seen in Fig. 3. Beginning with Al/Fe₂O₃ [Fig. 3(a)], upon initiation, the reaction temperature is ~ 2400 K and has a significant delay of ~ 1.5 ms. The temperature is seen to rise gradually over ~ 2 ms, reaching a

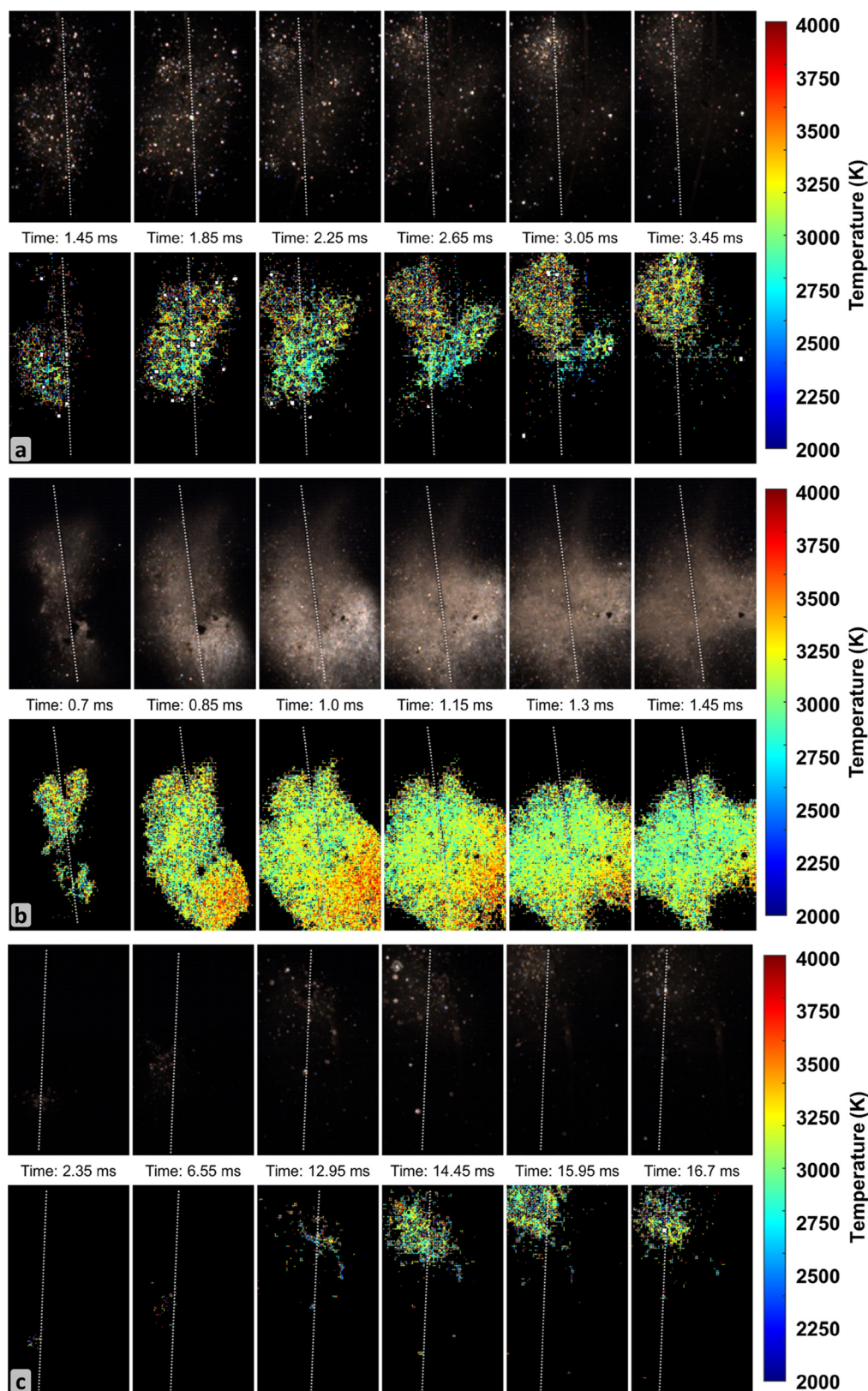


FIG. 5. High speed pyrometry frames of (a) Al/Fe₂O₃, (b) Al/Fe₂O₃/70% WO₃, and (c) Al/WO₃ samples ignited on a hot wire at a 1 atm argon environment highlighting the gas production and enhanced reaction. In the Al/WO₃ case, the reaction propagated up the wire over a longer time scale due to lack of gas release from the oxidizer. In each figure, the top image is a gain-adjusted raw image and the bottom image is the 2-D temperature map.

peak at ~ 3500 K, and dropping gradually thereafter for over 6 ms. The burn time observed for Al/Fe₂O₃ was the longest of the samples studied with the average FWHM burn time being approx. 6 ms, as shown in Fig. 4(c). Gaseous oxygen is

initially released by Fe₂O₃ at approximately 1400K (Ref. 21) and the combustion of the nanothermite is believed to be limited by the oxidizer decomposition, since complete decomposition to Fe occurs at (~ 3300 K).²¹

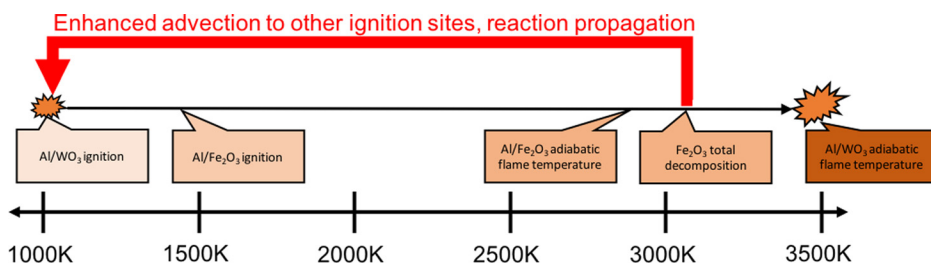


FIG. 6. Proposed reaction mechanism.

With addition of WO_3 , the initial reaction temperature of the sample rises by approximately 500 K to ~ 3000 K and is observed for all compositions containing WO_3 . We believe the similarities in temperature is due to the aluminum initiating with WO_3 , as it has a lower ignition temperature (1030 K vs. 1410 K),⁸ leading to a higher “initiation spot” temperature comparable with that of pure Al/ WO_3 . This initial enhancement in temperature could significantly improve the gasification of Fe_2O_3 , which could help in disaggregating the sample as highlighted by the increase in the pressure and pressurization rate in Fig. 4(b). Although the initial temperatures are higher, the concentration of WO_3 in the blend could be too low to influence the entire composite, hence only limited improvement in pressure was noticed. With further addition of WO_3 , the temperature does not change significantly, although the pressure metrics show improvement. The average temperatures in Fig. 4(a) are observed to plateau at ~ 3400 K, close to the adiabatic flame temperature of Al/ WO_3 (3447 K) and above the complete decomposition point, shown thermodynamically, of Fe_2O_3 .²¹

Comparing the measured temperatures to those of the theoretical estimates, it is observed that the predicted temperature profile rises slowly with incremental addition of WO_3 until a sharp rise at Al/ Fe_2O_3 /90 WO_3 , as opposed to the measured data which more or less plateaus at ~ 3400 K with the addition of WO_3 . The observed temperatures were also higher than the theoretical estimates as well as the average temperatures for Al/ Fe_2O_3 (~ 3100 K) suggesting heightened oxidizer decomposition. The lack of direct correlation between theoretical and measured values highlights the competing dynamics of the condensed phase reaction between Al- WO_3 and the gas phase reaction between Al- Fe_2O_3 . Recent work from our group³⁴ suggested that nanothermite reactions with a larger amount of gas release tend toward a more complete reaction due to disaggregation of the material, preventing active reactants from coalescing. The enhanced gas release observed in this work for the Al/ Fe_2O_3 / $x\text{WO}_3$ composite suggests that the composite is achieving a higher extent of reaction, resulting in shorter combustion time. Thus, the enhanced gas release could create a feedback loop where the composite disaggregation and convective heat transfer are promoted thereby increasing reactivity, as pictorially represented in Fig. 6.

As suggested in Fig. 6, ignition of Al/ WO_3 (which occurs at 1030 K) brings the mixture to a temperature at which oxygen release in Fe_2O_3 is initially observed (1400 K).⁸ The subsequent disaggregation of the material due to oxygen release then contributes to a more complete combustion of the Al/ WO_3 that approaches the adiabatic

flame temperature of the mixture at 3447 K, at which point the temperature exceeds the total decomposition point of Fe_2O_3 .²¹ The Fe_2O_3 decomposition into its suboxides (Fe_3O_4 , FeO , and Fe)¹⁴ then releases more gaseous oxygen, leading to further disaggregation of the material and propagation of the cycle. This is exemplified by the color camera pyrometry videos in Fig. 5, where the Al/ Fe_2O_3 /70% WO_3 composites exhibit a larger flame cloud with a higher temperature. Moreover, the reaction is observed to occur away from the wire highlighting the disaggregation effects of gas release.

As the temperatures exceeds full decomposition temperatures of Fe_2O_3 (~ 3300 K),²¹ a cloud of oxygen gas could be generated in which any residual aluminum, which could have coalesced into larger particle sizes, could now react. The high temperatures, observed for the doped composites approaching ~ 3800 K, similar to that of micron aluminum combustion in oxygen,³² could be suggestive of such a mechanism. The resulting figure of temperature and pressure as a function of oxidizer composition (Fig. 4) therefore illustrates a complex interplay between the WO_3 content (which elevates the temperature) and Fe_2O_3 (which elevates pressure through release of gaseous oxygen). This trend continues until a tipping point near 80% WO_3 , where the disaggregation through oxygen release from the Al/ Fe_2O_3 reaction is not able to influence the bulk of the composite, owing to Fe_2O_3 now being the minor component, suggesting a deviation from the optimal composition, in spite of the temperature profile showing similar features. When the composite is entirely WO_3 , the high temperature regions (~ 3800 K), observed for the doped composites, are no longer observed and the temperature is close to the adiabatic flame temperature of the Al/ WO_3 reaction (3447 K).²¹

V. CONCLUSIONS

The reactivity of metastable intermolecular composites was investigated through high speed spectrometry, pressure measurements, and color camera pyrometry, culminating in a proposed reaction mechanism for a tunable thermite reaction. Seven mixtures of Al/ Fe_2O_3 were doped with varying amounts of WO_3 to manipulate the primary reaction mechanism from gas-generating (Fe_2O_3) to condensed-phase (WO_3). While the pressure, pressurization rate, and burn time correlate with the mixture fraction, the temperature was relatively insensitive once a threshold addition of WO_3 was achieved. Pyrometry videos capture the interplay of reaction mechanisms of the doped thermite mixtures as evidenced by an enlarged reactive cloud size and faster reaction times with increasing amounts of WO_3 up to the 70% mark. It is

proposed that initiation by Al/WO₃ reactions leads to a greater degree of reduction of Fe₂O₃. The high oxygen release also results in flame temperatures in excess of the Al/Fe₂O₃ adiabatic flame temperature and reflects the burning of Al in an oxygen environment. The relative interplay between condensed and gas phase combustion suggests that performance of nanoenergetic materials can be tuned for specific applications by means of complementary reaction mechanisms.

SUPPLEMENTARY MATERIAL

See [supplementary material](#) for the calibration data for the spectrometer and pyrometer, pressure cell temperature data, as well as the schematic of the wire-ignition pyrometry apparatus.

ACKNOWLEDGMENTS

This work was supported by the Army Research Office.

- ¹D. D. Dlott, *Mater. Sci. Technol.* **22**, 463 (2006).
- ²M. R. Zachariah, *Propellants, Explos., Pyrotech.* **38**, 7 (2013).
- ³D. Sundaram, V. Yang, and R. A. Yetter, *Prog. Energy Combust. Sci.* **61**, 293 (2017).
- ⁴C. E. Aumann, G. L. Skofronick, and J. A. Martin, *J. Vac. Sci. Technol. B* **13**, 1178 (1995).
- ⁵G. C. Egan and M. R. Zachariah, *Combust. Flame* **162**, 2959 (2015).
- ⁶R. J. Jacob, G. Jian, P. M. Guerieri, and M. R. Zachariah, *Combust. Flame* **162**, 258 (2015).
- ⁷K. T. Sullivan, N. W. Piekielek, C. Wu, S. Chowdhury, S. T. Kelly, T. C. Hufnagel, K. Fezzaa, and M. R. Zachariah, *Combust. Flame* **159**, 2 (2012).
- ⁸G. Q. Jian, S. Chowdhury, K. Sullivan, and M. R. Zachariah, *Combust. Flame* **160**, 432 (2013).
- ⁹H. Wang, R. J. Jacob, J. B. DeLisio, and M. R. Zachariah, *Combust. Flame* **180**, 175 (2017).
- ¹⁰S. B. Kim, K. J. Kim, M. H. Cho, J. H. Kim, K. T. Kim, and S. H. Kim, *ACS Appl. Mater. Interfaces* **8**, 9405 (2016).
- ¹¹X. Zhou, M. Torabi, J. Lu, R. Q. Shen, and K. L. Zhang, *ACS Appl. Mater. Interfaces* **6**, 3058 (2014).
- ¹²R. J. Jacob, B. Wei, and M. R. Zachariah, *Combust. Flame* **163**, 281–289 (2016).
- ¹³R. Thiruvengadathan, A. Bezmelnitsyn, S. Apperson, C. Staley, P. Redner, W. Balas, S. Nicolich, D. Kapoor, K. Gangopadhyay, and S. Gangopadhyay, *Combust. Flame* **158**, 964 (2011).
- ¹⁴L. Zhou, N. Piekielek, S. Chowdhury, and M. R. Zachariah, *J. Phys. Chem. C* **114**, 14269 (2010).
- ¹⁵S. Zhang and E. L. Dreizin, *J. Phys. Chem. C* **117**, 14025 (2013).
- ¹⁶B. S. Bockmon, M. L. Pantoya, S. F. Son, B. W. Asay, and J. T. Mang, *J. Appl. Phys.* **98**, 064903 (2005).
- ¹⁷S. H. Fischer and M. C. Grubelich, in *32nd AIAA/ASME/SAE/ASEE Joint Propulsion Conference* (1996).
- ¹⁸V. E. Sanders, B. W. Asay, T. J. Foley, B. C. Tappan, A. N. Pacheco, and S. F. Son, *J. Propul. Power* **23**, 707 (2007).
- ¹⁹M. R. Weismiller, J. G. Lee, and R. A. Yetter, *Proc. Combust. Inst.* **33**, 1933 (2011).
- ²⁰K. Kappagantula, C. Crane, and M. Pantoya, *Propellants, Explos., Pyrotech.* **39**, 434 (2014).
- ²¹K. Sullivan and M. R. Zachariah, *J. Propul. Power* **26**, 467 (2010).
- ²²W. L. Perry, B. C. Tappan, B. L. Reardon, V. E. Sanders, and S. F. Son, *J. Appl. Phys.* **101**, 64313 (2007).
- ²³D. Ng and G. Fralick, *Rev. Sci. Instrum.* **72**, 1522 (2001).
- ²⁴T. Fu, Z. Wang, and X. Cheng, *J. Heat Transfer* **132**, 51602 (2010).
- ²⁵*Theory and Practice of Radiation Thermometry*, edited by D. P. DeWitt and G. D. Nutter (John Wiley & Sons, Inc., Hoboken, NJ, USA, 1988).
- ²⁶J. Kalman, D. Allen, N. Glumac, and H. Krier, *J. Thermophys. Heat Transfer* **29**, 74 (2015).
- ²⁷S. Goroshin, D. L. Frost, J. Levine, A. Yoshinaka, and F. Zhang, *Propellants, Explos., Pyrotech.* **31**, 169 (2006).
- ²⁸P. Lynch, G. Fiore, H. Krier, and N. Glumac, *Combust. Sci. Technol.* **182**, 842 (2010).
- ²⁹J. M. Densmore, M. M. Biss, K. L. McNesby, and B. E. Homan, *Appl. Opt.* **50**, 2659 (2011).
- ³⁰D. C. Morton, *Astrophys. J. Suppl. Ser.* **149**, 205 (2003).
- ³¹G. C. Egan, T. LaGrange, and M. R. Zachariah, *J. Phys. Chem. C* **119**, 2792 (2015).
- ³²P. Bucher, R. A. Yetter, F. L. Dryer, T. P. Parr, and D. M. Hanson-Parr, in *Twenty-Seventh Symposium on Combustion* (1998), Vol. 1, p. 2421.
- ³³K. T. Sullivan, O. Cervantes, J. M. Densmore, J. D. Kuntz, A. E. Gash, and J. D. Molitoris, *Propellants, Explos., Pyrotech.* **40**, 394 (2015).
- ³⁴R. J. Jacob, D. L. Ortiz-Montalvo, K. R. Overdeep, T. P. Weihs, and M. R. Zachariah, *J. Appl. Phys.* **121**, 054307 (2017).